# Amorphous Built-in-Field Effect Photoreceptors

JAPANESE JOURNAL OF APPLIED PHYSICS
VOL. 21, NO. 2, FEBRUARY, 1982 pp. 213–223

*—Invited Paper—*

# Amorphous Built-in-Field Effect Photoreceptors

Eiichi MARUYAMA

*Central Research Laboratory, Hitachi, Ltd., Kokubunji, Tokyo 185*

(Received November 12, 1981; accepted for publication November 21, 1981)

Thin-film photodiodes with the graded-composition structures of amorphous Se–As–Te have been developed. The physical mechanism of the buit-in-field effect in these highly resistive photodiodes has been clarified. In order to realize complicated composition distributions, multi-layer evaporation technology has also been developed. The physical properties of multi-layered films and those of the uniform amorphous film have been compared, and it has been shown that a multi-layered film of 1 nm periodicity can be regarded as an almost uniform amorphous material. Built-in-field effect photoreceptors can be utilized not only for TV pickup tubes but also for highly sensitive xerographic plate and other solid-state sensors.

## §1. Introduction—A Historical Background

Selenium was one of the earliest semiconductors to achieve practical applications. Selenium rectifiers and photocells were the predecessors of germanium or silicon diodes and solar cells, though the selenium material had been used in polycrystalline form in contrast with the single crystalline form of tetrahedral semiconductors.

In amorphous form, selenium is also known as one of the first practical photoconductors for xerographic plates[1] and experimental vidicon pickup tubes.[2] These devices are still playing major roles in information processing or image technology.

In contrast, amorphous pure tetrahedral material such as Si and Ge, as well as microcrystalline ones, have been shown to be poor photoconductors. These materials contain a large density of dangling bonds or grain boundaries that act as recombination centers or carrier traps. In 1975, Spear and LeComber found that these localized states are drastically reduced in glow-discharge produced amorphous silicon,[3] and that even p-n junction is possible to be formed by doping boron or phosphorous impurities into this material.[4] Amorphous hydrogenated silicon has, since then, become a *real* semiconductor material that is expected to have many practical applications, such as in solar cells,[5] vidicons,[6] xerographic plates[7] and thin-film transistors.[8]

The concept of dangling-bond termination in amorphous hydrogenated silicon can also be applied to microcrystalline tetrahedral materials. Hamasaka *et al.*[9] and Matsuda *et al.*[10] have shown that glow-discharge produced amorphous hydrogenated silicon that contains microcrystalline shows very high doping efficiency. The parallelism between amorphous or polycrystalline selenium and amorphous or polycrystalline hydrogenated silicon is now becoming more distinct in spite of their different bonding coordinations, that is, in two-dimentional selenium and tetrahedral silicon. Because of its rigid spatial structure, amorphous silicon needs dangling-bond terminators such as hydrogen atoms, while flexible amorphous selenium does not need such terminators to reduce its dangling bonds.

Formation of p-n junction in hydrogenated amorphous silicon has already been ascertained.[4] However, no reliable report on p-n junction formation in amorphous selenium has appeared, whereas a few papers on conductivity modulation in amorphous chalcogenides have attracted some attention.[11–13] The reasons seem to be that it is difficult to obtain n-type amorphous selenium and amorphous selenium has too low a bulk conductivity for the investigation of junction characteristics.

Classical selenium rectifiers are known to have the heterostructure of n-type CdSe and p-type polycrystalline selenium. There is the possibility of obtaining junction characteristics, therefore, in the heterostructure of some n-type material and amorphous selenium, though we must also take into account the very low bulk conductivity of a-Se, which is in the order of $10^{-14}\,\Omega^{-1}\,\mathrm{cm}^{-1}$.

The present paper deals with the formation of Se-rich amorphous chalcogenide thin-film photodiodes and their application to TV pickup tubes and other photosensors. Though this work was first reported[13–15] before the success of p-n junction formation in amorphous silicon, the operating mechanism of this amorphous chalcogenide photodiode has not yet been fully explained. The present paper is an attempt to give an overview of the physical properties and characteristics of this amorphous semiconductor diode.

## §2. Thin-Film Diodes and Blocking Layer

In conventional Schottky barrier diodes, it is assumed that the ohmic counter electrode to the semiconductor has no significant effect on the barrier characteristics of the Schottky contact. This is not the case in low-conductivity thin-film semiconductors. Figure 1 shows the band diagram for a p-type thin-film Schottky-barrier diode. A potential barrier for holes is formed between metal electrode, $M_1$, and the semiconductor,

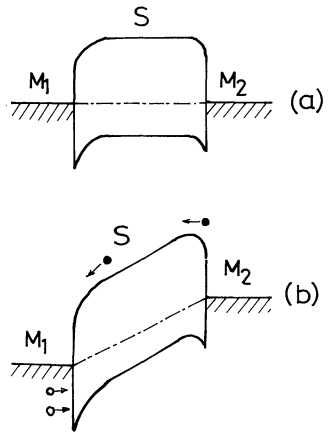


Fig. 1. Band models for a thin-film Schottky-barrier diode. $M_1$, $M_2$: Metal electrodes. S: p-type semiconductor. (a) Without applied voltage. (b) With applied voltage.

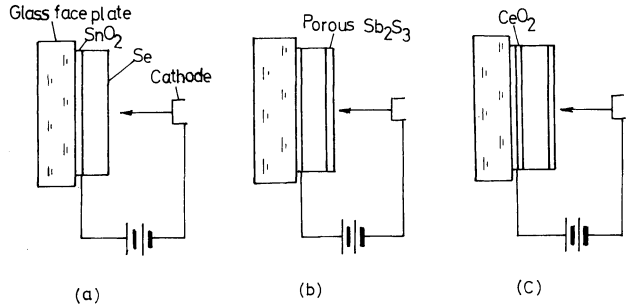


Fig. 2. Blocking-type vidicon targets of selenium photoconductor. (a) Only holes are blocked. (b) Both electrons and holes are blocked. (c) Hole-blocking is reinforced by $CeO_2$ insertion.

S, while the counter electrode, $M_2$, is assumed to be ohmic to the semiconductor. When reverse bias is applied to the Schottky barrier, as in Fig. 1(b), hole injection from $M_1$ is of course blocked by the barrier, but electron injection from $M_2$ is not. Moreover, because semiconductor S is highly resistive and very thin, a density of excess electrons far beyond thermal equilibrium can be injected into the semiconductor from $M_2$. If $\mu_e \tau_e E$ is larger than the thickness of the semiconductor, the reverse characteristics of this diode are destroyed by this excess electron current, where $\mu_e$, $\tau_e$ and $E$ are electron mobility, electron lifetime and electric field, respectively.

The most primitive selenium vidicon target is shown schematically in Fig. 2. On a glass substrate, an $SnO_2$ transparent electrode is deposited by chemical vapor deposition, or some other method. On top of this layer, a pure Se film about 2 $\mu$m thick is deposited by vacuum deposition. A rectifying barrier is thus formed between the n-type SnO and the p-type a-Se.

In ordinary vidicon operation, the transparent electrode is biased positively to the scanning electron beam to reverse-bias the rectifying barrier. The low velocity scanning beam ($\sim$1 eV) lands on the surface of the photoconductive target, and become uniform surface charge which will produce internal electric field in the highly resistive photoconductor. When the effective resistance of the photoconductor is much higher than the electron beam resistance, the surface potential of the photoconductor can be regarded as nearly same as that of the cathode. When the photoconductor is illuminated, the surface charge is modulated by the photogenerated carriers during the scanning period. The average surface potential during illumination, therefore, is different from that of the cathode. But if the amplitude of this potential modulation is small compared with the total voltage applied to the photoconductor, the surface potential again can be regarded as approximately same as that of the cathode. This potential amplitude $\Delta V$ is estimated from

$$\Delta V \simeq \tau_s (i_{ph}/C_t),$$

where $\tau_s$, $i_{ph}$ and $C_t$ are the scanning period, the photocurrent and the target capacitance, respectively. In ordinary operation, $\Delta V$ is about 2 volts. Thus, at low light levels, vidicon can be regarded as a kind of sandwich-type photoconductive cell.

Dark- and photocurrent in the vidicon target shown in Fig. 2 do not show complete saturation characteristics, however, and the decay time of the photocurrent is sometimes as large as hundreds milliseconds, reflecting a large carrier lifetime due to trapping. Moreover, the photocurrent in this type of target easily shows negative characteristics above a certain target voltage, as is shown in Fig. 3(a). This is due to secondary electron emission from the scanning surface of the target.

These drawbacks can be avoided if we deposit a porous $Sb_2S_3$ layer, as thin as 100 nm, on top of the a-Se layer, as is shown in Fig. 2(b). This layer prevents secondary electron emission owing to its porous structure and also acts as a blocking layer for electrons from scanning beam impinging into the conduction band of the a-Se. Photocurrent-voltage characteristics for a typical target of this type are shown in Fig. 3(b).

More complete saturation of the photocurrent is obtained by inserting a hole-blocking layer between the $SnO_2$ and Se as is shown in Fig. 2(c). In this case, the blocking layer is a $CeO_2$ film several tens of nm in thickness.

Figure 2(c) is the basic structure of our thin-film amorphous chalcogenide diode. Hole and electron

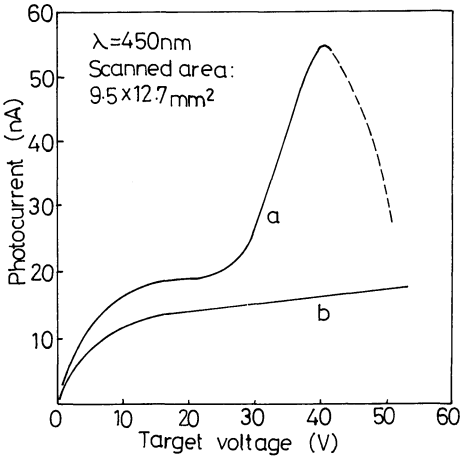


Fig. 3. Current-voltage characteristics of a Se-target vidicon. (a) Type-a target from Fig. 2. (b) Type-b target.

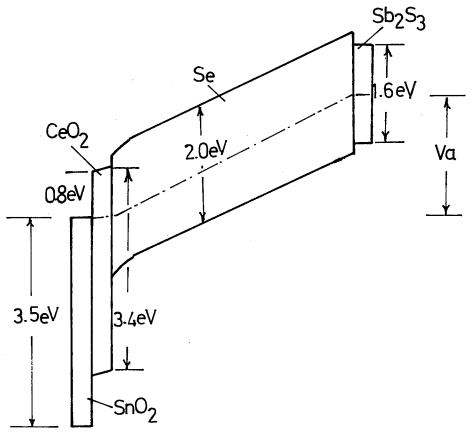


Fig. 4. Band model for the basic structure of a Se blocking target.

injections are blocked by $CeO_2$ and $Sb_2S_3$ layers, respectively. The blocking mechanisms in these two layers, however, are different from each other. Figure 4 shows a band diagram of this thin-film diode. Cerium oxide is an n-type wide-gap material and forms a large potential barrier to holes, whereas electrons can flow freely through the $CeO_2$–Se interface. The antimony trisulfide layer, on the other hand, has a narrower gap than a-Se, but it contains a large number of electron traps. Most of the electrons injected from the scanning beam are trapped in this layer and form a negative space-charge barrier. Photogenerated holes in the a-Se layer drift into the $Sb_2S_3$ layer and recombine with the trapped electrons in this layer.

In this basic structure of blocking photodiode, the decay time constant, $\tau_{ph}$, of the photocurrent is usually determined by

$$\tau_{ph} \sim d/\mu_h E,$$

where $d$ is the thickness of the photoconductor and $E$ is the electric field in the photoconductor. The value of $\tau_{ph}$ can be much less than that of excess majority carrier lifetime $\tau_h$, which determines the decay time in an injection type photoconductive cell. Thus, the blocking photodiode has characteristics similar to those of a p-i-n photodiode: fast photoresponse, low dark current, small junction capacitance, high breakdown voltage etc.

In an amorphous heterostructure, the lattice mismatch is not as serious a problem as in crystalline heterojunctions. This is thought to be due to the flexible structure of two-dimentionally coordinated a-Se. This flexibility increases the number of varieties of amorphous heterostructure photodiodes.

## §3. Improvement of Thermal Stability and Spectral Photoresponse

From a practical point of view, a-Se blocking photo- have two major drawbacks: crystallization of the selenium and insufficient red sensitivity.

Amorphous selenium is considered to be a random mixture of eight-member rings and large molecular chains of Se atoms. It gradually transforms itself into

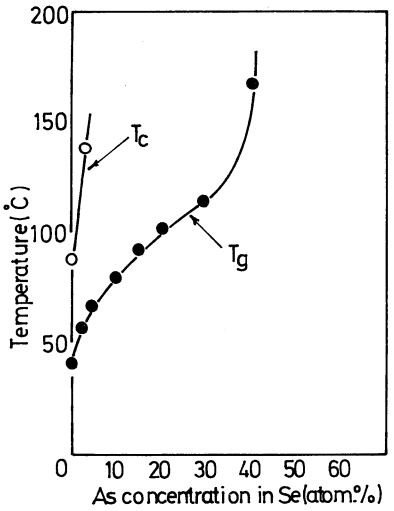


Fig. 5. Thermal properties of Se–As alloys. $T_c$: Crystallization temperature. $T_g$: Glass-transition temperature.

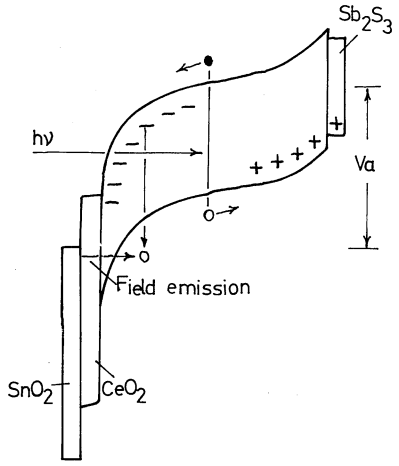


Fig. 6. Internal field modulation by trapped carriers in high trap-density materials.

trigonal microcrystalline even at room temperature. As the bulk resistivity of the trigonal selenium decreases to about $10^5$–$10^6$ Ω cm, the local dark current of the crystallized area of the photodiode increases greatly. This causes white blemishes in the video images, if the diode is used as a vidicon target.

The addition of arsenic to a-Se increases the crystallization temperature and the glass transition temperature of the material, as is shown in Fig. 5. And the addition of tellurium to a-Se enhances photosensitivity, especially in the long wavelength region.[16]

These additives, however, have undesirable effects on the transport properties of a-Se. They increase carrier traps in the material and lower the effective carrier mobilities by several orders of magnitude. Moreover, they destroy the blocking characteristics of the photodiode, especially when illuminated by long-wavelength light. This breakdown mechanism can be explained as shown in Fig. 6. In a blocking photodiode, the photogenerated carriers are separated by the applied electric field, and electrons flow toward the transparent electrode (forward) while holes flow the opposite way (backward). If the bulk material involves a large density of carrier

traps, negative carriers accumulate near the front electrode while positive carriers accumulate at the rear of the photoconductor. Recombination of these carriers rarely occurs, because these trapped carriers can not find their recombination counterparts, unless the latter are injected through the blocking electrodes. Thus, in a trap-rich blocking photodiode, a very high internal electric field is built up near the contacts due to the trapped space charge. This finally causes breakdown of the blocking characteristics of the diode. This breakdown is reversible and occurs in two ways. One is a uniform breakdown resulting in an increase in dark current. The other is a local breakdown, which causes "twinkling effect" in images produced by the device.

## §4. Graded Composition Photodiodes

In order to enhance the red sensitivity of a-Se blocking photodiode without increasing the number of harmful carrier traps which destroy the blocking characteristics or reduce carrier mobilities, we tried local addition of Te to the a-Se. The concentration of Te has to be low at the blocking contact with the $CeO_2$ layer, because this region is very sensitive to negative space-charge accumulation. The average concentration of Te in the a-Se bulk should also be low to keep from reducing carrier mobilities or causing long decay lag in the photocurrent. The best profile for Te distribution, therefore, may be to have Te atoms concentrated *near* the transparent electrode, where mostly incident light is absorbed, but not *at* the blocking contact.

Two types of Te concentration that might satisfy these requirements are shown in Fig. 7. Figure 7(a) is a square distribution and (b) is triangular. A vidicon target with type-a distribution, however, has strange characteristics. The video image taken by this target vanishes very rapidly in spite of constant illumination. This effect is due to instability of the photocurrent in this type of target.

The mechanism for this instability is internal polarization. Pure crystalline Te has a very narrow energy gap of about 0.3 eV. Although it is not easy to obtain amorphous Te film, it can be assumed that amorphous Te has nearly the same mobility gap width as crystalline Te. Further assuming that the mobility gap, $E_g$, in an amorphous $Se_xTe_{1-x}$ alloy can be described as $E_g = E_g(\mathrm{Se})x + E_g(\mathrm{Te})(1-x)$, the band models of the above photoconductive films can be presented as shown in

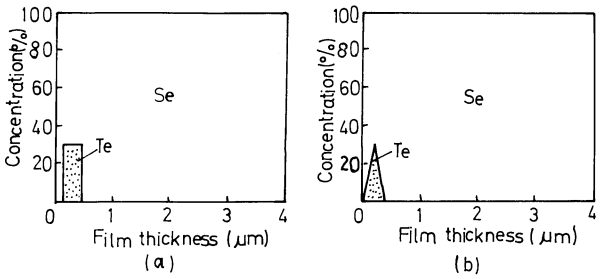


Fig. 7. Two types of Te distribution which might not destroy hole-blocking characteristics.

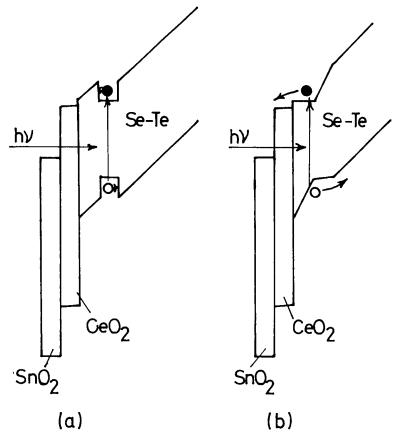


Fig. 8. Band models for the target proposed in Fig. 7.

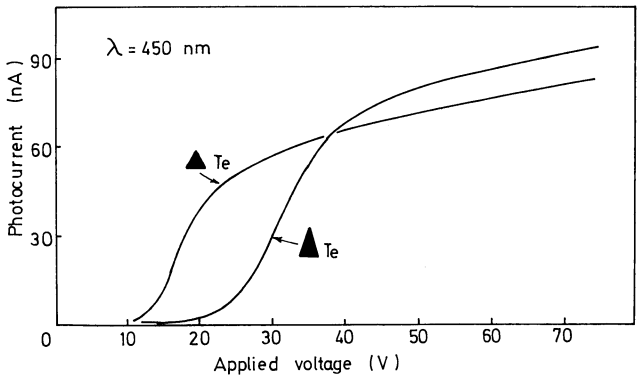


Fig. 9. Photocurrent-voltage characteristics of Te-doped selenium vidicon targets.

Fig. 8. The type-a distribution of Te forms potential wells both in the conduction and valence bands. The absorption of incident light occurs primarily in this region. Photogenerated electrons and holes, however, are confined in the potential well and form a dipole layer in the steady state. Thus, external photocurrent is hardly observed after the formation of the dipole layer. There are some experimental evidences that both electrons and holes are confined in these potential wells. In type-b distribution of Te, the potential well is triangular, and the photogenerated carriers in this region can be extracted by application of a sufficiently high electric field to compensate the internal field caused by band-narrowing.

The photocurrent-voltage characteristics of a type-b target are shown in Fig. 9. There is a threshold voltage, $V_{th}$, for each photocurrent build-up. These $V_{th}$'s can be described as the values of the applied voltage necessary to just compensate for the internal electric field. The width and height of the triangular Te concentration, therefore, determines the value of $V_{th}$. In Fig. 9, the target with the steeper Te distribution slope shows the higher $V_{th}$.

Thus, this photoconductive target is composed of four parts:

1) A hole-blocking region, which consists of a $CeO_2$ layer and a relatively high-purity a-Se layer.

2) A photosensitive region, which has a triangular

distribution of Te.

3) A capacitive region, which reduces the electrical capacity of the target through connection of a small series capacitance. This region is important because it reduces capacitive lag of the target.

4) An electron-blocking region, which consists of a porous $Sb_2S_3$ layer.

The above target structure is favorable to optimization of the operating characteristics of a pickup tube. Dark current is subjected to the properties of the blocking regions for both electrons and holes. Sensitivity is determined by the Te concentration, and capacitive lag is dependent on the thickness of the capacitive region. Thus, these characteristics can practically be designed and controlled separately.

## §5. Characteristics of Saticon® Pickup Tube

The graded-composition amorphous chalcogenide photodiode introduced in the previous section is the basic structure of the photoconductive target in the Saticon®, now widely utilized as a TV camera tube for broadcast, industrial and homeuse.[17]

Because of its grainless, uniform material structure, this target has very high resolving power. Figure 10 shows the amplitude response of an 18 mm-type Saticon®. This response is limited not by the target material itself, but by the scanning electron beam, and higher response can be obtained by improving the electron gun.

Figure 11 shows the spectral photosensitivity of the Saticon®, compared with that of a pure selenium target. The improvement in longer wavelength sensitivity is clearly shown. This spectral sensitivity can be designed, to some extent, by choosing a proper height and width of Te distribution. This feature is favorable for obtaining "ideal" spectral photoresponse for color image pickup, because in color TV cameras it is desirable to obtain well-balanced red, green and blue signal currents for three color channels. The spectral photoresponse in Fig. 11 may seem to have a relative sensitivity in the blue region that is too high compared with that of the red region. It should be noted, however, that the spectral energy distribution of illumination in a studio shows much higher energy in the red region than in the blue region. Thus, the resulting spectral signals in this pickup tube are averaged.

The lag characteristics of this pickup tube are quite good. This means that the capacitive lag which comes from the CR time constant of the target capacitance and scanning beam resistance has been reduced by the capacitive region introduced in the target, as was explained in the previous section, and that the photoconductive lag of this material is also low, due to the blocking structure of the target and to the low density of trapping levels in this material. Further reduction of lag is possible through the use of uniform bias light, which reduces the effective contact resistance of the scanning electron beam and the effective density of carrier traps in the target material.

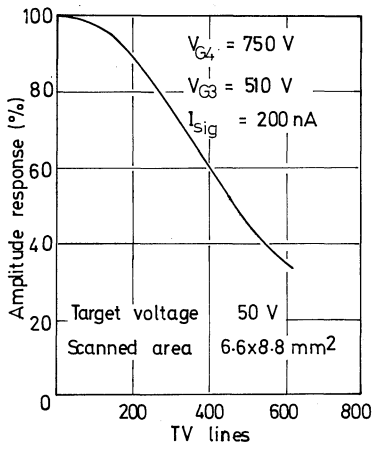


Fig. 10. Amplitude response of an 18 mm Saticon®.

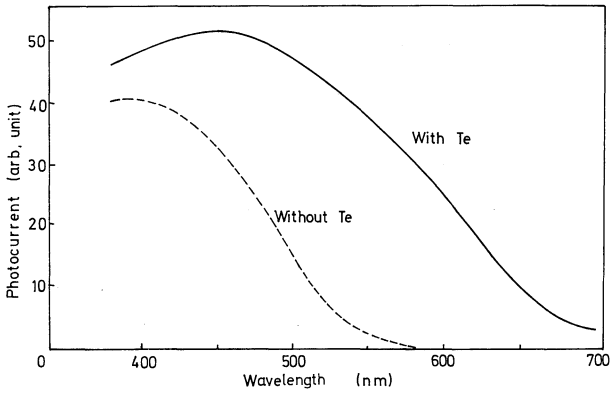


Fig. 11. Effect of Te-addition to the spectral photoresponse of a Se vidicon target.

The dark current level is as low as $\sim 0.3$ nA/cm$^2$ at room temperature. Thus, a very high signal-to-noise ratio can be obtained compared with conventional vidicons with injection-type $Sb_2S_3$ photoconductive targets, whose dark currents are as high as $\sim 20$ nA/cm$^2$ and sometimes have lateral non-uniformities which degrade video-picture quality.

## §6. Built-in-Field Effect Structure

In graded-composition photodiodes, it is desirable that the effective field in the photosensitive region be as high as possible. Since localized states or carrier traps are concentrated in this region, photogenerated carriers are easily immobilized and become fixed space charges which modulate the local electric field and cause a gradual increase or decrease in photocurrent. A higher electric field may prevent the formation of such undesirable space charges. Too high an applied voltage, however, would increase secondary electron emission at the back surface in a pickup tube.

Several new photodiode structures have been proposed to improve photocurrent stability.[18] Figure 12 shows two examples of them. In Fig. 12(b), half of the Te triangle in (a) is replaced by arsenic. Since arsenic forms deep electron traps in a-Se, this As-doped layer will act as a space-charge sheet with the trapped electrons thermally generated in the a-Se bulk or injected

from the scanning beam as a leakage dark current. Thus a built-in high electric field is established between this space-charge region and the hole-blocking contact with $CeO_2$.

The effect of this built-in field is remarkable. The total amount of Te for a certain value of photocurrent is reduced compared with the amount needed in the former triangular-Te structure, and photocurrent drift is reduced, as shown in Fig. 13. Even better photocurrent stability is obtained with the structure shown in Fig. 12(c), because the width of the Te-doped region is further reduced.

The density of the arsenic composition in the space-charge region in type-b and type-c targets should decrease gradually toward the back, to avoid making a potential step at the boundary with the capacitive region. In type-b and type-c targets, there may be potential steps between the Te-doped photosensitive regions and As-doped space-charge regions because arsenic is less effective in reducing the mobility gap width of a-Se than Te is. The accumulation of photogenerated holes at these potential steps, however, does not seem to have much effect on the stability of the photocurrent. This may be the evidence that the photogenerated holes flow rather smoothly out of the photosensitive region, through localized states produced by the arsenic atoms, into the conduction band of the a-Se of the capacitive region, with the assistance of the high, local electric field.

Figure 14 shows a proposed band diagram for a type-c target. This structure has a higher photosensitivity in the long wavelength region than the type-b target does, because the high Te-concentration region is closer to the light-incident surface. This structure, however, clearly has a potential step for photogenerated electrons, as is shown in the figure. There are also some experimental evidences of negative charge accumulation at this step. However, these carriers can be extracted by high electric field emission similar to the Poole-Frenkel effect.

The instability of electron current in this structure has little influence on the total current, because the photogenerated electrons have traverse-lengths as short as only about 1/100 of those of holes.

## §7. Multi-Layer Evaporation

The sophisticated film structure introduced in the previous sections can be produced by multi-source, high-precision evaporation technology.[19-22] The cross-sectional view of the evaporator, together with the block diagram of the computer-controlled system, is illustrated in Fig. 15. Substrates are placed near the periphery on a turn table rotating around an axis at *e.g.* 150 rpm. Several evaporation boats containing evaporation sources, such as Se, Te and $As_2Se_3$, are placed under the turn table. A common shutter and an independent shutter (opening controller) are inserted between each boat and the turn table.

The evaporation speeds of the evaporations from the

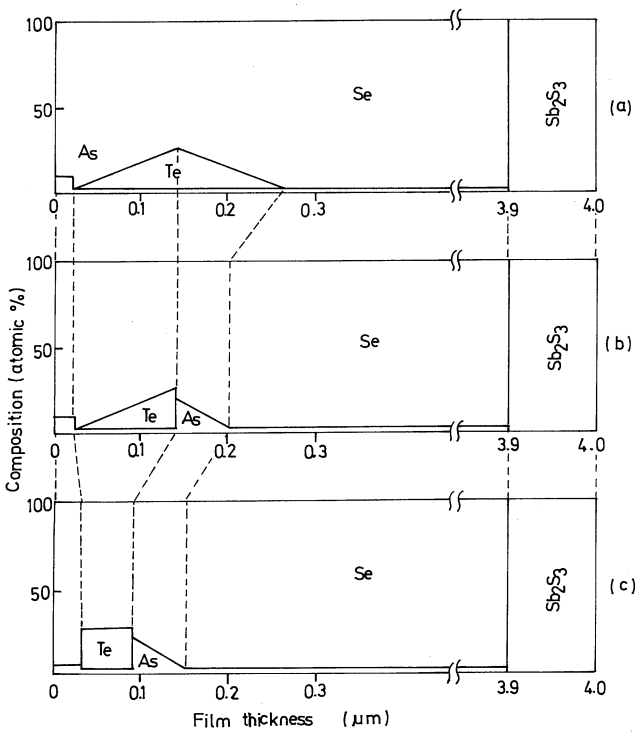


Fig. 12. Three types of Te and As distribution in Saticona targets.

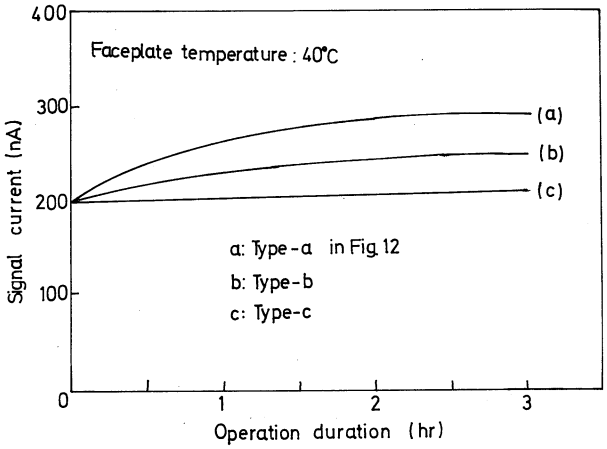


Fig. 13. Photocurrent drift of the targets shown in Fig. 12.

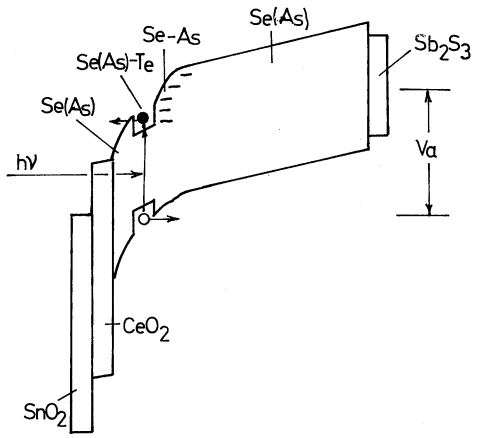


Fig. 14. Band model for a built-in-field effect target.

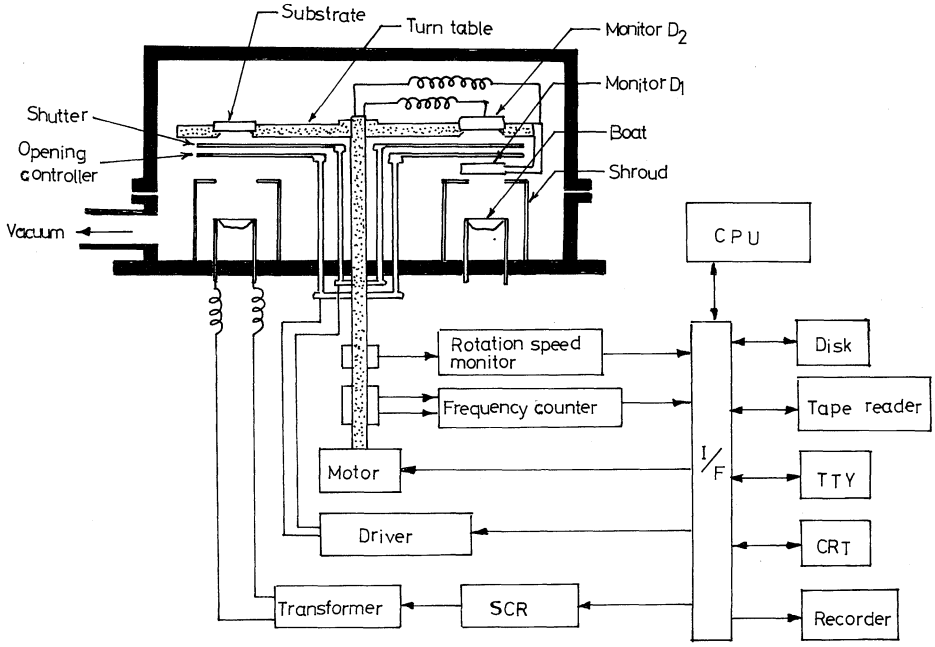


Fig. 15. Construction of a computer-controlled, multi-layer evaporation system.

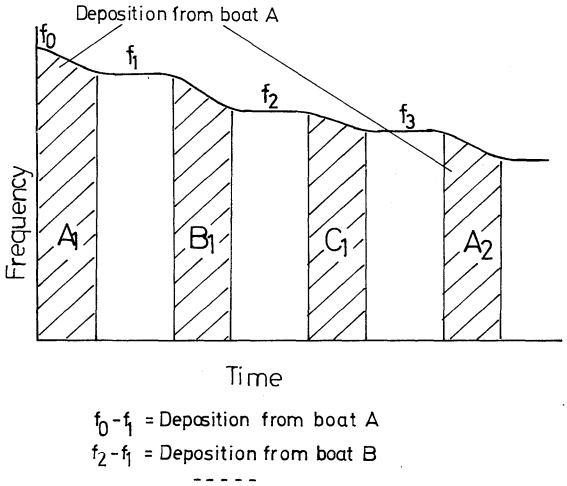


Fig. 16. Methods of thickness monitoring.

boats are detected time-sequentially by a quartz monitor, $D_1$, which is attached to the turn table and passes through the gap between the boats and the opening controllers. The principle for thickness measurement is illustrated in Fig. 16. The oscillation frequency of the quartz monitor changes from $f_0$ to $f_1$ when the monitor passes over one evaporation boat-A, and from $f_1$ to $f_2$ after passing over the next boat, B. Thus, $f_0-f_1=f_{A1}$ is the frequency change due to deposition from boat A for one turn, and $f_1-f_2=f_{B1}$ is that due to deposition from boat B for one turn. The total thickness of the deposition from boat A can be calculated from $f_A=f_{A1}+f_{A2}+\cdots+f_{An}$, while that from boat B can be calculated from $f_B=f_{B1}+f_{B2}+\cdots+f_{Bn}$, where $f_A, f_{A2}, \cdots f_{An}$ are the frequency changes due to the first, second, $\cdots$ and n-th turn of deposition from boat A, and so on. In this way, the evaporation speed for each boat can be detected separately, using one quartz monitor, a digital frequency counter and a computer system. These signals are fed back to the boat-current controller and the evaporation speed from each boat is held constant throughout the deposition process.

Another quartz monitor, $D_2$, is placed on the turn table in the same position as the substrates. This monitor time-sequentially detects the actual deposition speed and composition ratio. The thickness signals from this monitor are fed back to the opening controllers. The shutters control the opening of each boat to obtain the previously programmed composition ratio on the substrate.

By using separate sets of evaporators for the Se, Te and $As_2Se_3$, each structure of the targets shown in Fig. 12 can easily be deposited. This evaporation system can be used not only for laboratory experiments but also for mass-production of pickup tubes.

Films deposited by this method, however, are not uniform mixtures of amorphous materials. If we use separate sets of evaporators for the Se, Te and $As_2Se_3$, the deposited film may have a multi-layer structure of Se–Te–$As_2Se_3$–Se–Te–$As_2Se_3$–$\cdots$. Actually, the evaporation speed is slow, and the average thickness of a single layer of each component is less than 1 nm. However, whether this multi-layer film of amorphous materials has the same physical properties as a uniform or not should be investigated.

## §8. Physical Properties of Amorphous Multilayer Films

Amorphous chalcogenide materials are usually synthesized in evacuated quartz ampoules. The materials are melted and mixed for several hours in an electric furnace. Then the ampoules are water- or air-quenched, and the contents taken out.

However, the amorphous multi-layer films of the last section have quite different structures. They have even

periodic concentration profiles when they are deposited from multi-sources.

In order to investigate the physical properties of these multi-layer films, a simplified structure was chosen.[23] Figure 17 shows the basic structure of an experimental multi-layer film. The total thickness of the film is fixed at 2 $\mu$m, and the thickness, $\Delta t$, of a single layer of each component is changed as a parameter. Thus, if $\Delta t = 1$ $\mu$m, the film is composed of a 1-$\mu$m Se layer and a 1-$\mu$m $As_2Se_3$ layer. If $\Delta t = 100$ nm, the film is composed of ten 100-nm Se layers and ten 100-nm $As_2Se_3$ layers accumulated alternately. The average arsenic concentration in the film, therefore, is always 20 atomic %. Evaporated $As_{20}Se_{80}$ film using a source material which had been synthesized in a quartz ampoule was also prepared for comparison.

Figure 18 shows the optical transmission characteristics of these films. They show nearly the same optical properties, neglecting slight differences.

Figure 19 shows the temperature dependence of the electrical conductivity of these films. Evaporated gold electrodes were used for measurement. The current-voltage characteristics were nearly ohmic, except for the case of pure Se which showed an asymmetry. Electrical conductivity decreased and its activation energy increased, as $\Delta t$ increased. This may be due to the building-up of a contact barrier between the Se and $As_2Se_3$.

The thermal properties of these films were investigated using a differential scanning calorimeter. The results are shown in Fig. 20. In pure Se, an exothermal peak of crystallization and two endothermal peaks of glass transition and melting are observed. In the Se–As samples, however, only glass transition peaks are seen. When $\Delta t$ is 1 $\mu$m, two glass transition peaks appear at temperatures near those of pure Se and $As_2Se_3$. This shows that the two phases of Se and $As_2Se_3$ are separated. When $\Delta t$ decreases, these peaks come closer to each other until they finally coincide with each other at the glass transition temperature of $As_{20}Se_{80}$, although the two peaks remain separated even at $\Delta t = 1$ nm.

The above results are summarized in Fig. 21 as functions of $\Delta t$. The optical properties are almost unchanged, at least in the width of optical gap. The electrical properties show a large change between $\Delta t =$ 1 nm and $t = 30$ nm. Contact barriers between Se and $As_2Se_3$ may be completed in this thickness region. From thermal analysis, it can be said that the multi-layered film of $\Delta t = 1$ nm is almost uniform, but some micro-phase-separation still remains.

## §9. Application to Xerographic Photoreceptors and Other Devices

Recently, the need for highly resistive red- or infrared-sensitive photoconductive materials for diode-laser printers has been growing. Selenium-rich amorphous photoconductors are the most popular materials for xerography, but satisfactory long-wavelength sensitivity has yet to be achieved.

The amorphous built-in-field-effect photoreceptor

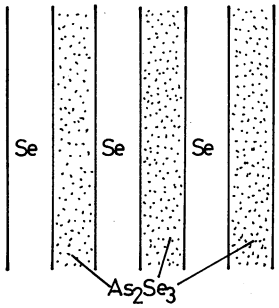


Fig. 17. Schematic cross section of experimental multi-layer of Se and $As_2Se_3$.

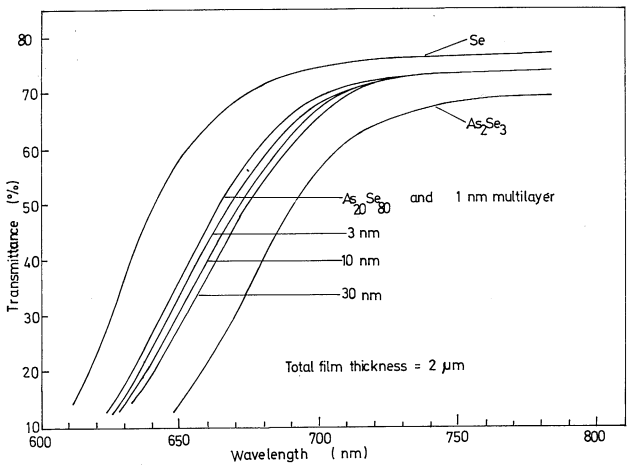


Fig. 18. Optical transmission of multi-layer films.

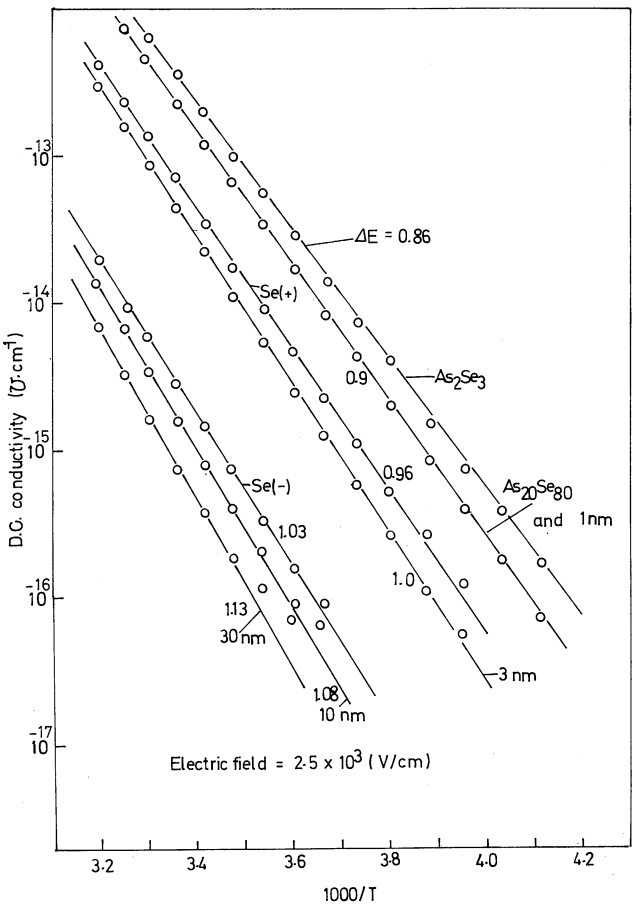


Fig. 19. Electrical conductivity of multi-layer films. E: Activation energy of the conductivity. T: Temperature.

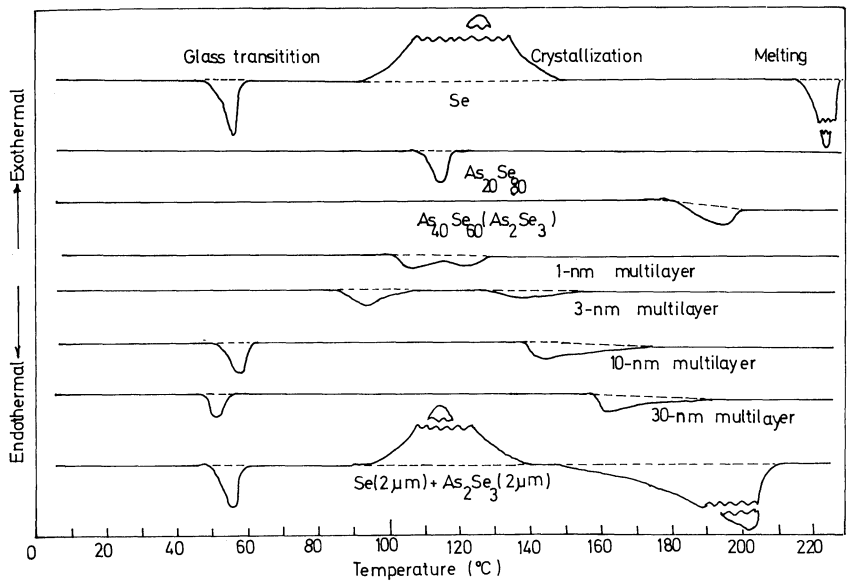


Fig. 20. Thermal properties of multi-layer films.

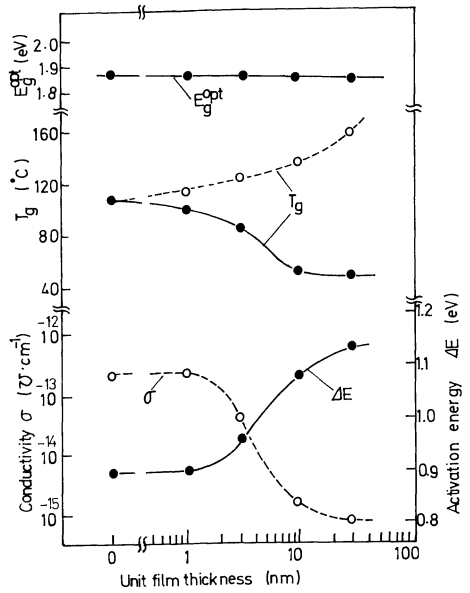


Fig. 21. Summary of optical, electrical and thermal properties of multi-layer films as functions of unit-layer thickness $\Delta t$. $E_g^{opt}$: Optical gap. $T_g$: Glass transition temperature. $\sigma$: Conductivity. $E$: Activation energy of the conductivity.

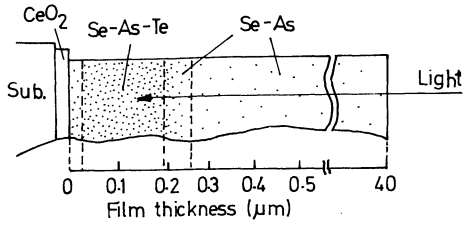


Fig. 22. Structure of a xerographic plate for a diode-laser printer.

introduced in this paper is considered to be one of the most promising candidates for use in a diode-laser photoconductor.[24] Figure 22 shows the proposed structure for the photoconductive film. A tellurium-doped photosensitive region is located near the sub-

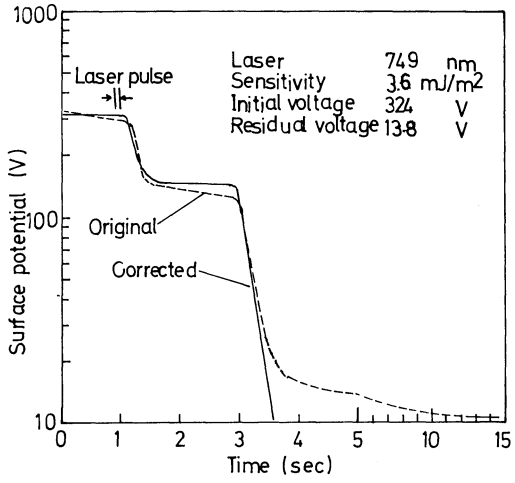


Fig. 23. Charge-decay characteristics of a built-in-field effect xerographic plate.

strate. Since the rest of the film is almost transparent to the diode laser wavelength, the incident light can reach the photosensitive region with little decay. The holes generated in the photosensitive region drift toward the surface of the film, while the electrons drift toward the substrate.

Figure 23 is the semi-logarithmic plot of surface potential decay of the photoconductor. The photoconductor is exposed to a 92.1 ms laser pulse at about 1 s, and to continuous laser light at about 3 s. The initial voltage is the potential at the time 0. The rate of dark decay is calculated from the approximate straight line in the semi-logarithmic plot during the period of the first 1 s. The residual voltage is defined as the surface potential estimated by extrapolation of the approximate straight line to time 0 in semi-logarithmic plot during the period between 12 and 15 s, when the photodecay almost disappears. The residual voltage is, therefore, an implicit non-decayable component in the surface potential by exposure. Purely photoconductive decay

can be calculated by extracting the dark decay and the residual potential decay from the original curve. This is shown in Fig. 23 as a corrected curve.

The photoconductive film in Fig. 23 has a photosensitivity of 3.6 mJ/cm$^2$ at 750 nm. This value is almost the same as that of pure Se at 442 nm. Moreover, it has high initial surface potential, low dark decay, low residual surface potential and good repetition stability.

Because the photosensitive region is embedded deep in the selenium film, the sensitivity of the film is hardly influenced by surface scratching or wearing. This is important for high-speed laser printing, in which photoconductive films are sometimes required to be used hundreds of thousands of times.

Other device applications for amorphous chalcogenide photodiodes have been proposed. Yamamoto *et al.*[25] have shown that this film has excellent characteristics for use as a contact-type linear photosensor for facsimile. Tsukada *et al.*[26] also have shown that it can be deposited on a two-dimentional scanner of silicon integrated circuits. This structure improves the aperture ratio of solid-state imagers and is quite effective in suppressing undesirable blooming or smearing.

The above examples show that this amorphous photodiode can be utilized in many types of photosensors, including pickup tubes and solid-state imagers. Since large-area uniformity is one of the most remarkable features of amorphous materials, such applications will be promising for amorphous photoconductive materials including both chalcogenide and hydrogenated silicon.

## §10. Conclusions

In this paper, I have tried to clarify the physical mechanism of amorphous chalcogenide built-in-field effect photoreceptors rather than to show data from individual experiments. The main points I would like to emphasize are as follows:

1) Selenium-rich amorphous chalcogenide can form heterostructure photodiodes as well as amorphous hydrogenated silicon. The junction formation in such amorphous materials depends on the density of the localized states involved. Selenium is the most *clean* amorphous chalcogenide in regard to electrical characteristics.

2) In a highly resistive photodiode structure, internal space-charge distribution plays a very important role in determining dynamic characteristics. Photocurrent instability is almost always caused by this space charge. However, trapped space charges, on the other hand, can be utilized to modify the internal electric field. This is effectively realized in built-in-field effect photodiodes.

3) Multi-layer evaporation technology has been developed to obtain graded-composition amorphous chalcogenide films. The amorphous materials thus deposited have almost the same physical properties as uniformly mixed materials when the average thickness of each elemental layer is less than 1 nm.

4) Amorphous built-in-field effect photoreceptors are now widely used as TV pickup tube targets. Additional uses as xerographic plates for diode-laser printers and other solid-state sensors have been proposed.

## Acknowledgements

The development of the Saticon® pickup tube has been carried out as a joint project of NHK Technical Research Laboratories and Hitachi, Ltd. The author would like to express his sincere thanks for the cooperation and valuable discussions of Drs. T. Ninomiya (at present, Toshiba Corporation), I. Oishi, N. Goto and many other members of NHK (Japan Broadcasting Corporation), and to Drs. M. Oikawa, T. Hirai, S. Otsuka, Y. Nonaka and the many other members of Hitachi, Ltd., who have been engaged in this long-term project for more than ten years.

## References

1) J. Mort and D. M. Pai: *Photoconductivity and Related Phenomena* (Elsevier Scientific Publishing Co., New York, 1976) p. 421.
2) P. K. Weimer and A. D. Cope: RCA Rev. **12** (1951) 314.
3) W. E. Spear and P. G. LeComber: Solid State Commun. **17** (1975) 1193.
4) W. E. Spear, P. G. LeComber, S. Kimmond and M. H. Brodsky: Appl. Phys. Lett. **28** (1976) 105.
5) D. E. Carlson and C. R. Wronski: Appl. Phys. Lett. **29** (1976) 602.
6) Y. Imamura, S. Ataka, Y. Takasaki, C. Kusano, T. Hirai and E. Maruyama: Appl. Phys. Lett. **35** (1979) 349.
7) I. Shimizu, T. Komatsu, K. Saito and E. Inoue: J. Non-Cryst. Solids **35** & **36** (1980) 773.
8) P. G. LeComber, W. E. Spear and A. Ghaith: Electron. Lett. **15** (1979) 181.
9) T. Hamasaki, M. Hirose, H. Kurata, M. Taniguchi and Y. Osaka: *Proc. 12th Conf. Solid State Devices, Tokyo 1980*, Jpn. J. Appl. Phys. **20** (1981) Suppl. 20–1, p. 281.
10) A. Matsuda, S. Yamasaki, K. Nakagawa, H. Okushi, K. Tanaka, S. Iizima, M. Matsumura and H. Yamamoto: Jpn. J. Appl. Phys. **19** (1980) L305.
11) W. A. LaCourse, V. A. Twaddell and J. D. Mackenzie: J. Non-Cryst. Solids **3** (1970) 234.
12) S. R. Ovshinsky: *Proc. 7th Int. Conf. Amorphous & Liquid Semiconductors, Edinburg 1977* (Univ. Edinburgh, Edinburgh, 1977) p. 519.
13) E. Maruyama, T. Hirai, T. Fujita, N. Goto, Y. Isozaki and K. Shidara: *Proc. 6th Conf. Solid State Devices, Tokyo 1974*, Oyo Buturi (J. Jpn. Soc. Appl. Phys.) **44** (1975) Suppl., p. 97.
14) E. Maruyama, T. Hirai, N. Goto, Y. Isozaki and K. Shidara: *Proc. 5th Int. Conf. Amorphous & Liquid Semiconductors, Garmisch 1973*, p. 581.
15) N. Goto, Y. Isozaki, K. Shidara, E. Maruyama, T. Hirai and T. Fujita: IEEE Trans. Electron Devices **EC-21** (1974) 662.
16) P. H. Keck: J. Opt. Soc. Am. **42** (1952) 221.
17) T. Ninomiya, K. Wakui, N. Goto and K. Shidara: NHK Tech. Monogr. No. 25 (1976).
18) K. Shidara, N. Goto, E. Maruyama, T. Hirai and Y. Nonaka: Electron Device Lett., **EDL-2** (1981) 101.
19) E. Maruyama, T. Hirai, K. Inao and N. Goto: US Patent 3800194 (Priority 1972).
20) T. Hirai, K. Inao, E. Maruyama, S. Koizumi, I. Sugita and S. Suzuki: Japan Patent 952116 (Filed 1972).
21) E. Maruyama, T. Hirai, S. Ishioka, H. Yamamoto and

K. Inao: US Patent 4121537 (Priority 1976).
22) T. Hirai, S. Ishioka, H. Yamamoto, Y. Mori and E. Maruyama: *Symp. Design of Inorganic & Organic Materials, Kyoto 1979*, eds. T. Yonezawa and T. Yamabe (Kyoto Univ., Kyoto, 1979).
23) H. Yamamoto, T. Hirai, E. Maruyama and Y. Hamakawa: Gakushin Hakumaku 84kai Kenkyukai Shiryo (Proc. 84th Meeting of Thin Film) (131th Commitee, Japan Society for the Promotion of Science, Tokyo, 1977) [in Japanese].
24) Y. Taniguchi, H. Yamamoto, S. Horigome, S. Saito and E. Maruyama: J. Appl. Phys. (1981).
25) H. Yamamoto, M. Matsui, T. Tsukada, Y. Eto, T. Hirai and E. Maruyama: *Proc. 9th Conf. Solid State Devices, Tokyo 1977*, Jpn. J. Appl. Phys. **17** (1978) Suppl. 17–1, p. 135.
26) T. Tsukada, T. Baji, H. Yamamoto, Y. Takasaki, T. Hirai, E. Maruyama S. Ohba, N. Koike, H. Ando and T. Akiyama: 1979 Int. Electron Devices Meet. Tech. Dig., p. 134.